Chapter 5

Measurement of Bispectrum on the *COBE* DMR sky maps

Several authors have attempted to measure non-Gaussianity in CMB using various statistical techniques (e.g., Kogut et al. 1996b); as yet no conclusive detection has been reported except for measurement of several modes of the normalized CMB bispectrum on the *COBE* Differential Microwave Radiometer (DMR) sky maps (Ferreira et al., 1998; Magueijo, 2000). The existence of non-Gaussianity in the DMR data is controversial. If the CMB sky were non-Gaussian, this would challenge our simplest inflationary model.

The angular bispectrum, $B_{l_1 l_2 l_3}$, is the harmonic transform of the three-point correlation function. We carefully distinguish the normalized bispectrum, $B_{l_1 l_2 l_3}/\left(C_{l_1} C_{l_2} C_{l_3}\right)^{1/2}$, from the bispectrum, $B_{l_1 l_2 l_3}$. Ferreira et al. (1998) have measured 9 equilateral ($l_1 = l_2 = l_3$) modes of the normalized bispectrum, $B_{l_1 l_2 l_3}/\left(C_{l_1} C_{l_2} C_{l_3}\right)^{1/2}$, on the DMR map, claiming detection at $l_1 = l_2 = l_3 = 16$. Their result has been under extensive efforts to confirm its significance and origin. Bromley and Tegmark (1999) claim that a few individual pixels in the DMR map are responsible for the most of the signal. Banday et al. (2000) have proposed an eclipse effect by the Earth against the *COBE* satellite as a possible source of the signal. Magueijo (2000) has measured other 8 inter-l modes of the normalized bispectrum such as $B_{l-1 l l+1}/\left(C_{l-1} C_l C_{l+1}\right)^{1/2}$, and claims that scatter of the normalized bispectrum among 8 modes is too small to be consistent with Gaussian. Sandvik and Magueijo (2000) further report measurement of 24 other inter-l modes for different lags in l, and conclude they are consistent with Gaussian.

Thus, until now 41 modes of the normalized bispectrum have been measured on the DMR map. Here, we simply ask: "how many modes are available in the DMR map for the bispectrum?" The answer is 466, up to a maximum multipole of 20 that corresponds to the DMR beam size; thus, it is conceivable that the claimed detection of the normalized bispectrum at $l_1 = l_2 = l_3 = 16$ would be explained by a statistical fluctuation, as 9 modes are expected to have statistical significance above 98% out of 466 independent modes even if CMB is exactly Gaussian. In this chapter, we measure 466 modes of the CMB bispectrum on the *COBE* DMR sky maps, testing the claimed detection of the bispectrum and non-Gaussianity. We take into account the covariance between these modes due to the Galactic cut, which has not been done in the previous work.

On the theoretical side, several predictions for the CMB bispectrum exist. Several authors (Falk et al., 1993; Luo and Schramm, 1993; Gangui et al., 1994) have predicted the primary bispectrum (or equivalently three-point correlation function) on the DMR angular scales from slow-roll inflation models. In chapter 4, we have extended the prediction down to arcminutes scales using the full radiation transfer function.

In addition to the primary one, secondary sources in the low-redshift universe and foreground sources produce the bispectrum through their non-linearity. Luo and Schramm (1993) and Spergel and Goldberg (1999) have calculated the secondary bispectrum arising from non-linear evolution of gravitational potential; Goldberg and Spergel (1999) and Cooray and Hu (2000) have calculated the one from the gravitational lensing effect coupled with various secondary anisotropy sources. In chapter 4, we have calculated the foreground bispectrum from extragalactic radio and infrared point sources. While the bispectrum is not the best tool for detecting the signature of rare highly non-linear events, e.g., textures (Phillips and Kogut, 2001), it is sensitive to weakly non-linear effects.

Having theoretical predictions is a great advantage in extracting physical information from measurement; one can fit a predicted bispectrum to the data so as to constrain parameters in a theory. Since the DMR beam size is large enough to minimize contribution from the secondary and the extragalactic foreground sources, the only relevant source would be the primary one. In this chapter, we fit a theoretical primary bispectrum (Komatsu and Spergel, 2001a) to the data.

The Galactic plane contains strong microwave emissions from interstellar sources. The emissions are highly non-Gaussian, and distributed on fairly large angular scales. Unfortunately, predicting the CMB bispectrum from interstellar sources is very difficult; thus, we excise the galactic plane from the DMR data. We model the residual foreground bispectrum at high galactic latitude using foreground template maps. By simultaneously fitting the foreground bispectrum and the primary bispectrum to the DMR data for three different Galactic cuts, we quantify the importance of the interstellar emissions in our analysis.

This chapter is organized as follows. In § 5.1, we define the angular bispectrum, and show how to compute it efficiently from observational data. In § 5.2, we study statistical properties of the bispectrum and the normalized bispectrum. We then measure the normalized bispectrum from the *COBE* DMR four-year sky maps (Bennett et al., 1996), testing Gaussianity of the DMR map. In § 5.3, we fit predicted bispectra to the DMR data, constraining parameters in the predictions. The predictions include the primary bispectrum from inflation and the foreground bispectrum from interstellar Galactic emissions. Finally, § 5.4 concludes.

5.1 Angular Bispectrum

The CMB angular bispectrum consists of a product of three harmonic transforms of the CMB temperature field. For Gaussian fields, expectation value of the bispectrum is exactly zero. Given statistical isotropy of the universe, the angular averaged bispectrum, $B_{l_1l_2l_3}$, is given by

$$B_{l_1l_2l_3} = \sum_{\text{all } m} \begin{pmatrix} l_1 & l_2 & l_3 \\ m_1 & m_2 & m_3 \end{pmatrix} a_{l_1m_1}a_{l_2m_2}a_{l_3m_3}, \tag{5.1}$$

where the matrix denotes the Wigner-3j symbol, and harmonic coefficients, a_{lm}, are given by

$$a_{lm} = \int_{\Omega_{\text{obs}}} d^2\hat{\mathbf{n}}\ \frac{\Delta T\left(\hat{\mathbf{n}}\right)}{T} Y_{lm}^*\left(\hat{\mathbf{n}}\right). \tag{5.2}$$

Ω_{obs} denotes a solid angle of the observed sky. $B_{l_1l_2l_3}$ satisfies the triangle condition, $|l_i - l_j| \le l_k \le l_i + l_j$ for all permutations of indices, and parity invariance, $l_1 + l_2 + l_3 = \text{even}$.

We can rewrite equation (5.1) into a more useful form. Using the identity,

$$\begin{aligned} \begin{pmatrix} l_1 & l_2 & l_3 \\ m_1 & m_2 & m_3 \end{pmatrix} &= \begin{pmatrix} l_1 & l_2 & l_3 \\ 0 & 0 & 0 \end{pmatrix}^{-1} \sqrt{\frac{(4\pi)^3}{(2l_1+1)(2l_2+1)(2l_3+1)}} \\ &\times \int \frac{d^2\hat{\mathbf{n}}}{4\pi}\ Y_{l_1m_1}(\hat{\mathbf{n}})Y_{l_2m_2}(\hat{\mathbf{n}})Y_{l_3m_3}(\hat{\mathbf{n}}), \end{aligned} \tag{5.3}$$

we rewrite equation (5.1) as

$$B_{l_1l_2l_3} = \begin{pmatrix} l_1 & l_2 & l_3 \\ 0 & 0 & 0 \end{pmatrix}^{-1} \int \frac{d^2\hat{\mathbf{n}}}{4\pi}\ e_{l_1}(\hat{\mathbf{n}})e_{l_2}(\hat{\mathbf{n}})e_{l_3}(\hat{\mathbf{n}}), \tag{5.4}$$

where the integral is not over Ω_{obs}, but over the whole sky; $e_l(\hat{\mathbf{n}})$ already encapsulates the information of incomplete sky coverage through a_{lm}. Following chapter 3, we used the azimuthally averaged harmonic transform of the CMB temperature field, $e_l(\hat{\mathbf{n}})$,

$$e_l(\hat{\mathbf{n}}) = \sqrt{\frac{4\pi}{2l+1}} \sum_m a_{lm}Y_{lm}(\hat{\mathbf{n}}). \tag{5.5}$$

Similarly, we write the angular power spectrum, C_l, as

$$C_l = \int \frac{d^2\hat{\mathbf{n}}}{4\pi}\ e_l^2(\hat{\mathbf{n}}). \tag{5.6}$$

Thus, $e_l(\hat{\mathbf{n}})$ is a square-root of C_l at a given position of the sky. Equation (5.4) is computationally efficient, as we can calculate $e_l(\hat{\mathbf{n}})$ quickly with the spherical harmonic transform for a given l. Since the HEALPix pixels have the equal area (Górski et al., 1998), the average over the whole sky, $\int d^2\hat{\mathbf{n}}/(4\pi)$, is done by the sum over all pixels divided by the total number of pixels, $N^{-1}\sum_i^N$.

5.2 Measurement of Bispectrum on the DMR Sky Maps

5.2.1 The data

We use the HEALPix-formatted (Górski et al., 1998) *COBE* DMR four-year sky map, which contains 12,288 pixels in Galactic coordinate with a pixel size 1.°83. We obtain the most sensitive sky

Table 5.1: Monopole and Dipole Subtraction

The monopole, T_0, and the dipole, T_1, anisotropies that have been subtracted from the DMR sky maps. We show the subtracted values for zero, 20°, 25°, and 30° cuts. The rightmost column shows the directions of the subtracted dipole in Galactic coordinate.

$\lvert b_{\rm cut}\rvert$	T_0 [μK]	T_1 [μK]	$\mathbf{T}_1/T_1$ (l, b)
0°	1.40	63.1	(28.°07, 2.°12)
20°	−70.3	26.2	(89.°23, −4.°17)
25°	−72.4	26.9	(84.°89, −5.°13)
30°	−73.4	28.6	(97.°32, −6.°31)

map to CMB by combining 53 GHz map with 90 GHz map, after coadding the channels A and B at each frequency. We do not subtract eclipse season time-ordered data; while Banday et al. (2000) ascribe the reported non-Gaussianity to this data, we will argue in this paper that the claimed detection of the normalized bispectrum at $l_1 = l_2 = l_3 = 16$ (Ferreira et al., 1998) can also be explained in terms of a statistical fluctuation.

We reduce interstellar Galactic emissions by using three different Galactic cuts: 20°, 25°, and 30° in Galactic latitude. Since we want to see how the different Galactic cuts affect the measured bispectrum, we use the three different Galactic cuts instead of the extended Galactic cut (Banday et al., 1997), which is commonly used for analyzing the DMR sky maps. Then, we subtract the monopole and the dipole from each cut map, minimizing contaminations from these two multipoles to higher order multipoles through the mode-mode coupling. The coupling arises from incomplete sky coverage. This is very important to do, for the leakage of power from the monopole and the dipole to the higher order multipoles is rather big. We use the least-squares fit weighted by the pixel noise variance to measure the monopole and the dipole on each cut map. Table 5.1 shows the amplitude of the subtracted monopole and the dipole for the different Galactic cuts.

We measure the bispectrum, $B_{l_1 l_2 l_3}$, on the DMR sky maps as follows. First, we measure a_{lm} using equation (5.2). Then, we transform a_{lm} for $-l \le m \le l$ into $e_l(\hat{\mathbf{n}})$ through equation (5.5). Finally, we obtain $B_{l_1 l_2 l_3}$ from equation (5.4), arranging l_1, l_2, and l_3 in order of $l_1 \le l_2 \le l_3$, where the maximum l_3 is set to be 20. In total, we have 466 non-zero modes after taking into account $|l_i - l_j| \le l_k \le l_i + l_j$ and $l_1 + l_2 + l_3 =$ even. Measurement of 466 modes takes about 1 second of CPU time on a Pentium-III single processor personal computer.

5.2.2 Monte–Carlo Simulations

We use Monte–Carlo simulations to estimate the covariance matrix of the measured bispectrum. Our simulation includes (a) a Gaussian random realization of the primary CMB anisotropy field drawn from the *COBE*-normalized ΛCDM power spectrum, and (b) a Gaussian random realization of the instrumental noise drawn from diagonal terms of the *COBE* DMR noise covariance matrix (Lineweaver et al., 1994). For computational efficiency, we do not use off-diagonal terms as they are smaller than 1% of the diagonal terms (Lineweaver et al., 1994).

We generate the input power spectrum, C_l, using the CMBFAST code (Seljak and Zaldarriaga, 1996) with cosmological parameters fixed at $\Omega_{\rm cdm} = 0.25$, $\Omega_\Lambda = 0.7$, $\Omega_{\rm b} = 0.05$, $h = 0.7$, and $n = 1$; the CMBFAST code uses the Bunn and White (1997) normalization.

In each realization, we generate a_{lm} from the power spectrum, multiply it by the harmonic-transformed DMR beam, G_l (Wright et al., 1994), transform $G_l a_{lm}$ back to a sky map, and add an instrumental noise realization to the map. Finally, we measure 466 modes of the bispectrum from each realization. We generate 50,000 realizations for one simulation; processing one realization takes about 1 second, so that one simulation takes about 16 hours of CPU time on a Pentium-III single processor personal computer.

5.2.3 Normalized bispectrum

The input power spectrum determines the variance of the bispectrum. Off-diagonal terms in the covariance matrix arise from incomplete sky coverage. When non-Gaussianity is weak, the variance is given by (Luo, 1994; Heavens, 1998; Spergel and Goldberg, 1999; Gangui and Martin, 2000)

$$\left\langle B^2_{l_1l_2l_3}\right\rangle = \left\langle C_{l_1}\right\rangle \left\langle C_{l_2}\right\rangle \left\langle C_{l_3}\right\rangle \Delta_{l_1l_2l_3}, \tag{5.7}$$

where $\Delta_{l_1l_2l_3}$ takes values 1, 2, or 6 for all l's are different, two are same, or all are same, respectively. The brackets denote the ensemble average.

The variance is undesirably sensitive to the input power spectrum; even if the input power spectrum were slightly different from the true power spectrum on the DMR map, the estimated variance from simulations would be significantly wrong, and we would erroneously conclude that the DMR map is inconsistent with Gaussian. It is thus not a robust test of Gaussianity to compare the measured bispectrum with the Monte–Carlo simulations.

The *normalized* bispectrum, $B_{l_1l_2l_3}/\left(C_{l_1}C_{l_2}C_{l_3}\right)^{1/2}$, is more sensible quantity than the bare bispectrum. Magueijo (1995) shows that the normalized bispectrum is a rotationally invariant spectrum independent of the power spectrum, as it factors out fluctuation amplitude in a_{lm}, which is measured by $C_l^{1/2}$. By construction, the variance of the normalized bispectrum is insensitive to the power spectrum, approximately given by $\Delta_{l_1l_2l_3}$.

One might wonder if the normalized bispectrum is too noisy to be useful, as the power spectrum in the denominator is also uncertain to some extent; however, we find that the variance is actually slightly smaller than $\Delta_{l_1l_2l_3}$. Figure 5.1 compares the variance of the normalized bispectrum, $\left\langle B^2_{l_1l_2l_3}/\left(C_{l_1}C_{l_2}C_{l_3}\right)\right\rangle$, with that of the bispectrum, $\left\langle B^2_{l_1l_2l_3}\right\rangle/\left(\left\langle C_{l_1}\right\rangle \left\langle C_{l_2}\right\rangle \left\langle C_{l_3}\right\rangle\right)$. The top-left panel shows the case of full sky coverage. We find that the variance of the normalized bispectrum is precisely 1 when all l's are different, while it is slightly smaller than 2 or 6 when two l's are same or all l's are same, respectively. This arises due to correlation between the uncertainties in the bispectrum and the power spectrum, and this correlation tends to reduce the total variance of the normalized bispectrum. The rest of panels show the cases of incomplete sky coverage. While the variance becomes more scattered than the case of full sky coverage, the variance of the normalized bispectrum is still systematically smaller than that of the bare bispectrum. Thus, the normalized bispectrum is reasonably sensitive to non-Gaussianity, yet it is not sensitive to the overall normalization of power spectrum.

What distribution does the normalized bispectrum obey for a Gaussian field? First, even for a Gaussian field, the probability distribution of a single mode of $B_{l_1l_2l_3}$ is non-Gaussian, characterized by a large kurtosis. Figure 5.2 plots the distributions of 9 modes of $B_{l_1l_2l_3}$ drawn from the Monte–Carlo simulations (solid lines) in comparison with Gaussian distributions calculated from r.m.s. values (dashed lines). We find that the distribution does not fit the Gaussian very well. Then, we examine distribution of the normalized bispectrum, $B_{l_1l_2l_3}/\left(C_{l_1}C_{l_2}C_{l_3}\right)^{1/2}$. We find that the distribution is very much Gaussian except for $l_1 = l_2 = l_3 = 2$. Figure 5.3 plots the distributions of the 9 modes of the normalized bispectrum (solid lines) in comparison with Gaussian distributions calculated from r.m.s. values (dashed lines). The distribution fits the Gaussian remarkably well; this motivates our using standard statistical methods developed for Gaussian fields to analyze the normalized bispectrum. We could not make this simplification if we were analyzing the bare bispectrum. Furthermore, the central limit theorem implies that when we combine 466 modes the deviation of the distribution from Gaussianity becomes even smaller.

Ferreira et al. (1998) claim detection of the normalized bispectrum at $l_1 = l_2 = l_3 = 16$; Magueijo (2000) claims that the scatter of the normalized bispectrum for $l_1 = l_2 - 1$ and $l_3 = l_2 + 1$ is too small to be consistent with Gaussian. The former has analyzed 9 modes, while the latter has analyzed 8 modes. In the next section, we analyze 466 modes, testing the statistical significance of the non-Gaussianity with much more samples than the previous work. We calculate C_l from equation (5.6), and then divide $B_{l_1l_2l_3}$ by $\left(C_{l_1}C_{l_2}C_{l_3}\right)^{1/2}$ to obtain the normalized bispectrum.

5.2.4 Testing Gaussianity of the DMR map

We characterize statistical significance of the normalized bispectrum as probability of the measured normalized bispectrum being greater than those drawn from the Monte–Carlo simulations. We define the probability P as

$$P_\alpha \equiv \frac{N\left(\left|I_\alpha^{\rm DMR}\right| > \left|I_\alpha^{\rm MC}\right|\right)}{N_{\rm total}} = \int_{-\left|I_\alpha^{\rm DMR}\right|}^{\left|I_\alpha^{\rm DMR}\right|} dx\ F_\alpha^{\rm MC}(x), \qquad (5.8)$$

where I_α is the normalized bispectrum, $N_{\rm total} = 50,000$ is the total number of simulated realizations, and $\alpha = 1,\ 2,\ 3,\ 4,\ldots,\ 466$ represent $(l_1, l_2, l_3) =$ (2,2,2), (2,3,3), (2,2,4), (3,3,4),…, (20,20,20), respectively, with satisfying $l_1 \le l_2 \le l_3$, $|l_i - l_j| \le l_k \le l_i + l_j$, and $l_1 + l_2 + l_3 = $ even. $F_\alpha^{\rm MC}(x)$ is the probability density distribution function (p.d.f) of the simulated realizations for the normalized bispectrum, $x = I_\alpha^{\rm MC}$. The p.d.f is normalized to unity: $\int_{-\infty}^{\infty} dx F_\alpha^{\rm MC}(x) = 1$; thus, P_α lies in $0 \le P_\alpha \le 1$.

By construction, the distribution of P_α is uniform, if the DMR map is consistent with the simulated realizations, i.e., Gaussian. We give the proof as follows. By rewriting equation (5.8) as $P_\alpha = f(\left|I_\alpha^{\rm DMR}\right|)$, we calculate the p.d.f of P_α, $G(P_\alpha)$, as

$$G(P_\alpha) \;=\; \int_{-\infty}^{\infty} dy\ \delta\left[P_\alpha = f(|y|)\right] F_\alpha^{\rm DMR}(y)$$

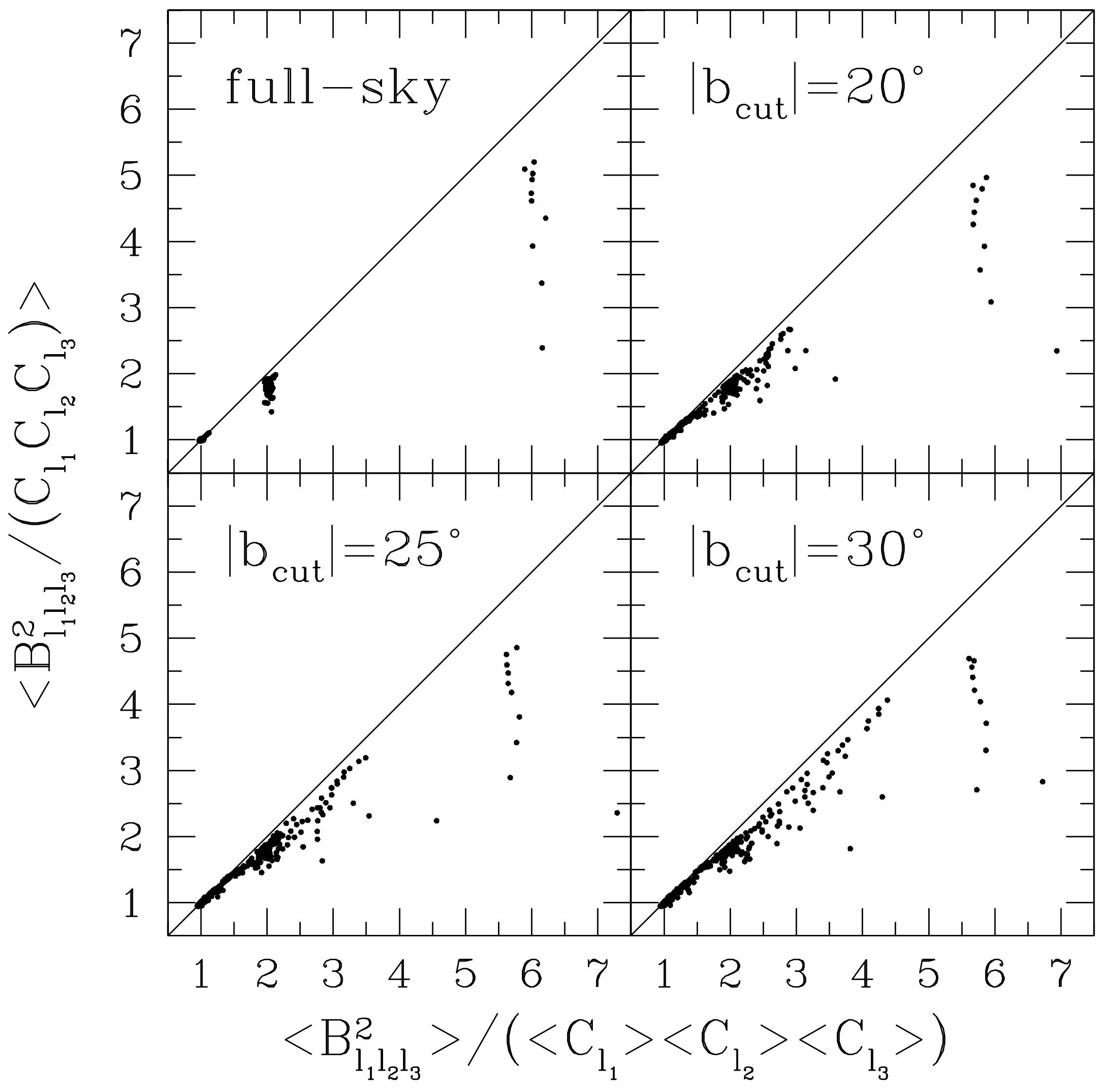

Figure 5.1: Variance of Normalized Bispectrum and Bare Bispectrum

Variance of the normalized bispectrum, $\left\langle B^2_{l_1l_2l_3}/\left(C_{l_1}C_{l_2}C_{l_3}\right)\right\rangle$, in comparison with variance of the bare bispectrum, $\left\langle B^2_{l_1l_2l_3}\right\rangle/\left(\left\langle C_{l_1}\right\rangle\left\langle C_{l_2}\right\rangle\left\langle C_{l_3}\right\rangle\right)$. These are derived from simulated realizations of a Gaussian sky. The top-left panel shows the case of full sky coverage, while the rest of panels show the cases of incomplete sky coverage. The top-right, bottom-left, and bottom-right panels use the 20°, 25°, and 30° Galactic cuts, respectively.

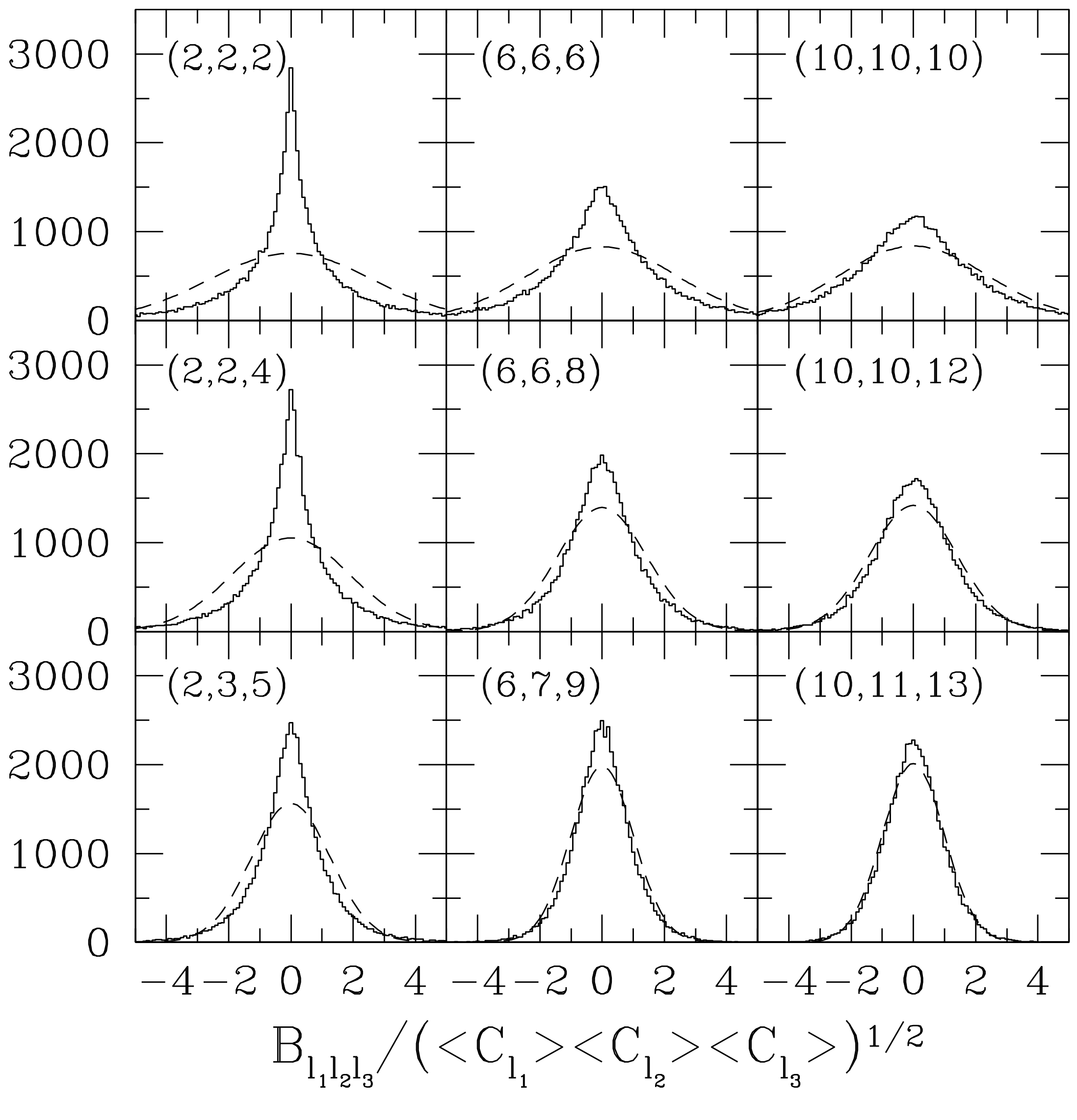

Figure 5.2: Distribution of Bispectrum

Distribution of the bare bispectrum drawn from the Monte–Carlo simulations (solid lines). The 20° Galactic cut is used. $B_{l_1 l_2 l_3}/\left(\langle C_{l_1}\rangle \langle C_{l_2}\rangle \langle C_{l_3}\rangle\right)^{1/2}$ is plotted, where the brackets denote the ensemble average over realizations from the Monte–Carlo simulations. The dashed lines plot Gaussian distributions calculated from r.m.s. values. Each panel represents a certain mode of (l_1, l_2, l_3) as quoted in the panels.

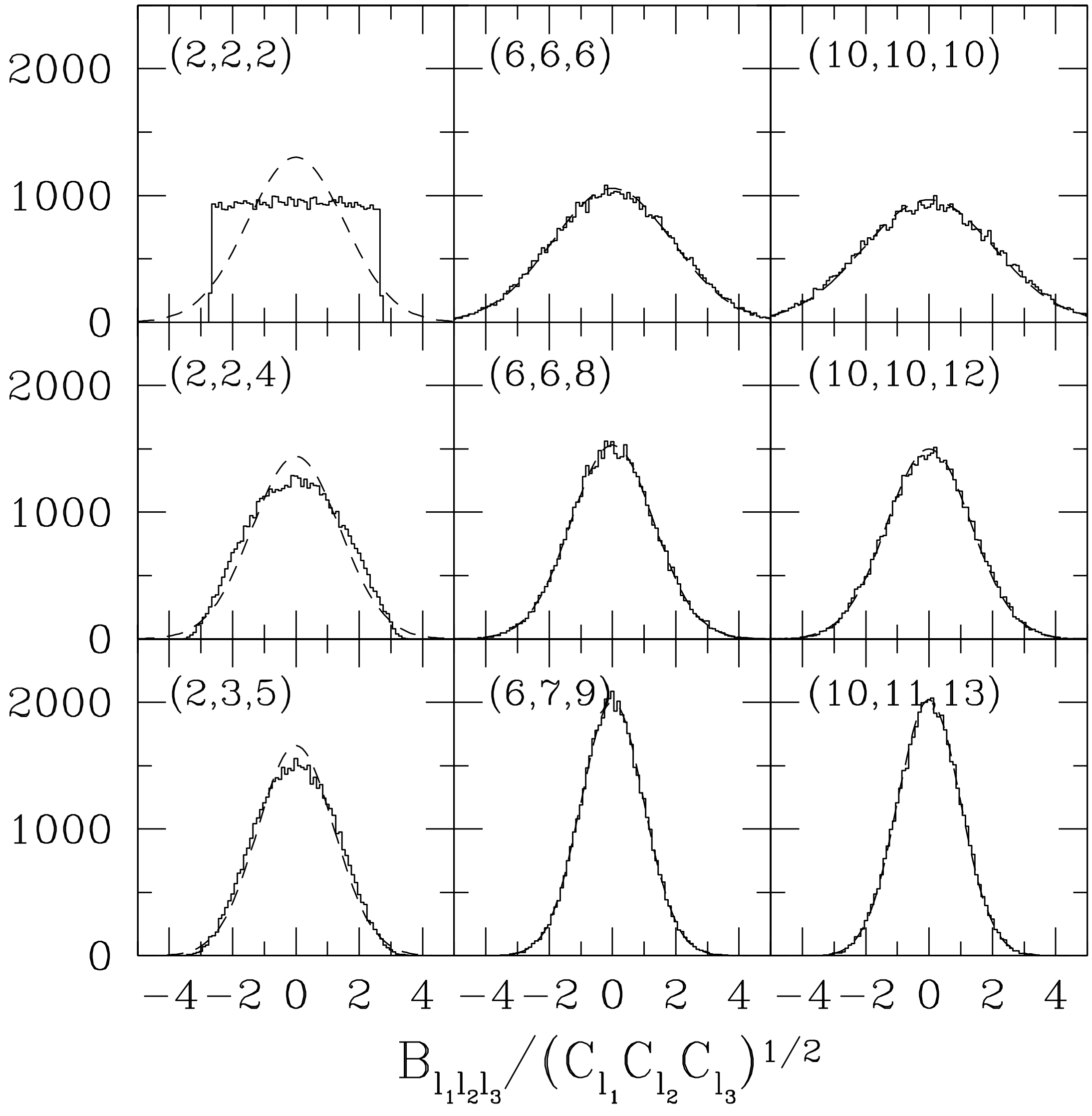

Figure 5.3: Distribution of Normalized Bispectrum

Distribution of the normalized bispectrum (solid lines), $B_{l_1l_2l_3}/\left(C_{l_1}C_{l_2}C_{l_3}\right)^{1/2}$, in comparison with Gaussian distributions calculated from r.m.s. values (dashed lines). The 20° Galactic cut is used. The meaning of the panels is the same as in figure 5.2.

$$
\begin{aligned}
&= \int_0^\infty dy\, \delta\left[P_\alpha = f(y)\right]\left[F_\alpha^{\mathrm{DMR}}(y) + F_\alpha^{\mathrm{DMR}}(-y)\right] \\
&= \int_0^\infty dy\, \frac{\delta\left[y = f^{-1}(P_\alpha)\right]}{df/dy}\left[F_\alpha^{\mathrm{DMR}}(y) + F_\alpha^{\mathrm{DMR}}(-y)\right] \\
&= \int_0^\infty dy\, \delta\left[y = f^{-1}(P_\alpha)\right]\frac{F_\alpha^{\mathrm{DMR}}(y) + F_\alpha^{\mathrm{DMR}}(-y)}{F_\alpha^{\mathrm{MC}}(y) + F_\alpha^{\mathrm{MC}}(-y)},
\end{aligned}
\tag{5.9}
$$

where $F_\alpha^{\mathrm{DMR}}(y)$ is the p.d.f of the measured normalized bispectrum on the DMR map, $y = I_\alpha^{\mathrm{DMR}}$. Our goal is to see if $F_\alpha^{\mathrm{DMR}}(y)$ is consistent with the DMR data being Gaussian. It follows from equation (5.9) that $G(P_\alpha) \equiv 1$, when $F_\alpha^{\mathrm{DMR}}(y) \equiv F_\alpha^{\mathrm{MC}}(y)$, regardless of the functional form of $F_\alpha^{\mathrm{MC}}(y)$. In other words, the distribution of P_α is uniform, if the distribution of the measured normalized bispectrum is the same as the simulated realizations. Since our simulation assumes the DMR map Gaussian, the P distribution, $G(P)$, tests the Gaussianity of the DMR map. If the P distribution is not uniform, then we conclude the DMR data to be non-Gaussian.

A Gaussian field gives equal number of modes in each bin of P. For example, it gives 46.6 modes in $\Delta P = 10\%$ bin: $466 \times G(P)\Delta P = 466 \times 0.1 = 46.6$. If we detect the normalized bispectrum significantly, then we find that $G(P)$ is not uniform, but increases rapidly as P increases.

The top panel of figure 5.4 plots the P distribution for the three different Galactic cuts. We find that the distribution is uniform, and the number of modes in the bin ($\Delta P = 10\%$) is consistent with the expectation value for Gaussian fluctuations (46.6).

To further quantify how well it is uniform, we calculate the Kolmogorov–Smirnov (KS) statistic for the P distribution in comparison with the uniform distribution. The bottom panel of figure 5.4 plots the cumulative P distribution, for which we calculate the KS statistic. The probability of the distribution being uniform is 6.7%, 77%, and 52% for the three Galactic cuts, respectively. While we have confirmed that the normalized bispectrum at $l_1 = l_2 = l_3 = 16$ has $P = 97.8\%$ for the 20° cut and $P = 99.3\%$ for the 25° cut as similar to Ferreira et al. (1998), our result shows that it is well within statistical fluctuations. Thus, the properties of the normalized bispectrum of the DMR map are consistent with CMB being a Gaussian field.

5.3 Model Fitting

In this section, we fit predicted CMB bispectra to the measured normalized bispectrum. The predictions include the primary bispectrum from inflation and the interstellar foreground bispectrum from the Galactic emissions. Then, we constrain a parameter characterizing the primary bispectrum.

5.3.1 Primary bispectrum

For the primary bispectrum from inflation, we consider weakly non-Gaussian adiabatic perturbations generated through non-linearity in slow-roll inflation. The simplest weak non-linear coupling gives

$$
\Phi(\mathbf{x}) = \Phi_{\mathrm{L}}(\mathbf{x}) + f_{\mathrm{NL}}\left[\Phi_{\mathrm{L}}^2(\mathbf{x}) - \left\langle \Phi_{\mathrm{L}}^2(\mathbf{x}) \right\rangle\right], \tag{5.10}
$$

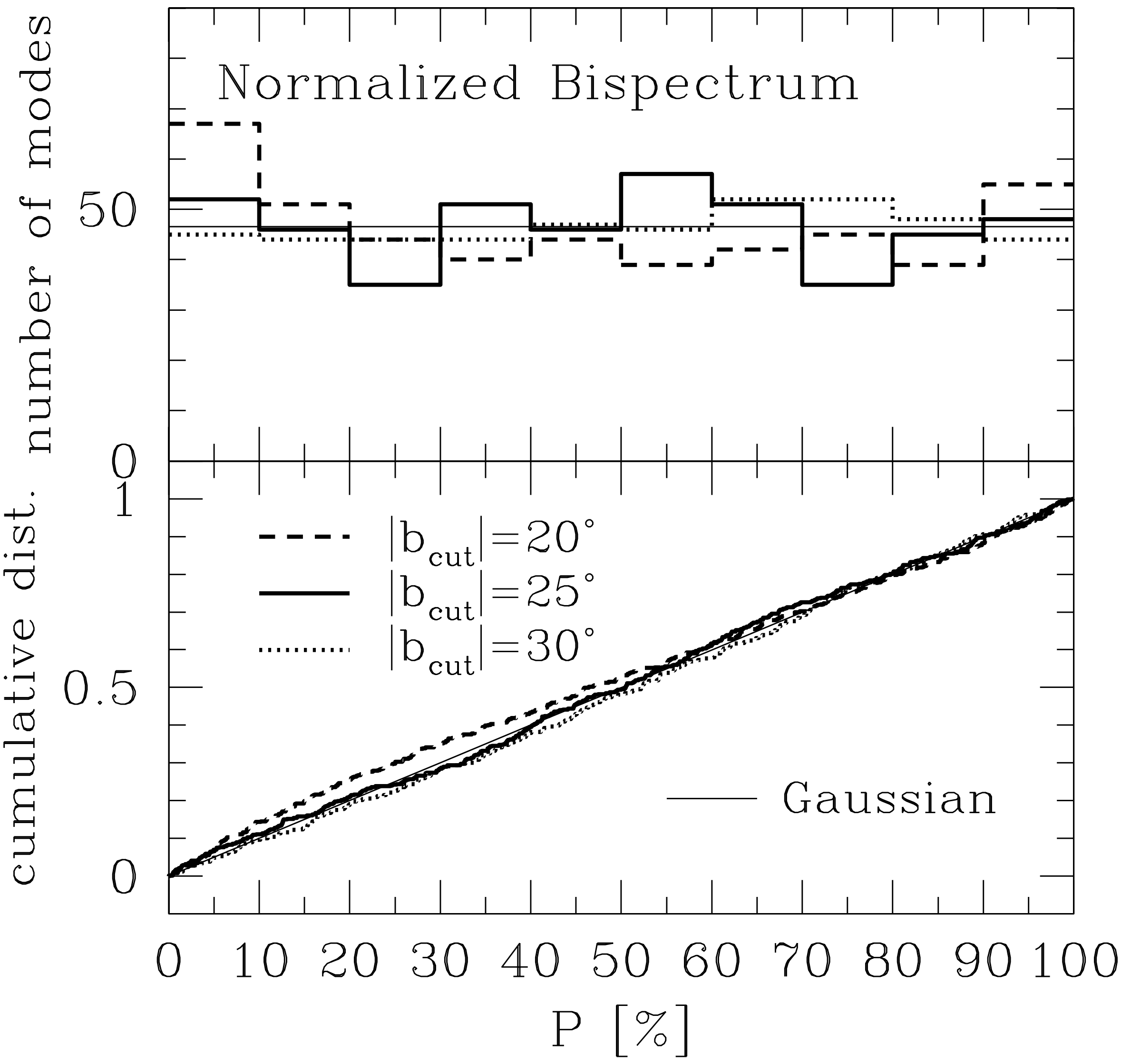

Figure 5.4: KS Test for Gaussianity with Bispectrum

P distribution (Eq.(5.8)). P is the probability of the CMB normalized bispectrum, $B_{l_1 l_2 l_3}/(C_{l_1} C_{l_2} C_{l_3})^{1/2}$, measured on the *COBE* DMR 53 + 90 GHz sky map, being larger than those drawn from the Monte–Carlo simulations. There are 466 modes in total. The thick dashed, solid, and dotted lines represent the three different Galactic cuts as quoted in the figure. The thin solid line shows the expectation value for a Gaussian field. The top panel shows the P distribution, while the bottom panel shows the cumulative P distribution, for which we calculate the KS statistic. The KS statistic gives the probability of the distribution being consistent with the expectation for Gaussianity as 6.7%, 77%, and 52% for the three Galactic cuts, respectively.

where the square bracket denotes the volume average, and $\Phi_{\rm L}(\mathbf{x})$ is a linear Gaussian part of curvature perturbations. We call $f_{\rm NL}$ the non-linear coupling parameter.

Salopek and Bond (1990, 1991) and Gangui et al. (1994) show that slow-roll inflation gives this coupling; Pyne and Carroll (1996) shows that the second-order general relativistic perturbation theory gives this. The former predicts $f_{\rm NL}$ as a certain combination of slope and curvature of a inflaton potential ($\Phi_3 = -2f_{\rm NL}$ in Gangui et al. (1994)). The latter predicts $f_{\rm NL} \sim \mathcal{O}(1)$. In chapter 4, we have given the exact form of $B_{l_1l_2l_3}$ for this model; we do not repeat it here. $f_{\rm NL}$ is the parameter that we try to constrain by measuring the CMB bispectrum.

Since the theoretical bispectrum assumes full sky coverage, we must correct it for the bias arising from incomplete sky coverage. We use an approximate correction factor for the bias, $\Omega_{\rm obs}/4\pi$, which we have derived in chapter 3. Moreover, the theoretical bispectrum must also be convolved with the DMR beam. We use the harmonic transform of the DMR beam, G_l, given in Wright et al. (1994). Hence, the observed bispectrum is related to the theoretical one through

$$B^{\rm obs}_{l_1l_2l_3} = \frac{\Omega_{\rm obs}}{4\pi} B^{\rm theory}_{l_1l_2l_3} G_{l_1} G_{l_2} G_{l_3}. \tag{5.11}$$

Note that $\Omega_{\rm obs}/4\pi = 1 - \sin|b_{\rm cut}|$ for an azimuthally symmetric cut within certain latitude $b_{\rm cut}$; $\Omega_{\rm obs}/4\pi = 0.658$, 0.577, and 0.5 for $|b_{\rm cut}| = 20^\circ$, 25°, and 30°, respectively.

5.3.2 Foreground bispectra from interstellar emissions

Although we cut a fraction of the sky to reduce interstellar emissions from the Galactic plane, there should be some residuals at high Galactic latitude. Kogut et al. (1996a) have found significant correlation between *COBE* DMR maps at high Galactic latitude and *COBE* Diffuse Infrared Background Experiment (DIRBE) maps which mainly trace dust emission from the Galactic plane.

The interstellar emissions are highly non-Gaussian. For example, the one-point p.d.f of the all-sky dust template map (Schlegel et al., 1998) is highly skewed. We find the normalized skewness, $\left\langle (\Delta T)^3 \right\rangle / \left\langle (\Delta T)^2 \right\rangle^{3/2} \sim 51$. Since these non-Gaussian emissions would confuse the parameter estimation of the primary CMB bispectrum, we take the effect into account.

We estimate the foreground bispectra from interstellar sources by using two foreground template maps. One is the dust template map of Schlegel et al. (1998); the other is the synchrotron map of Haslam et al. (1981). Both maps are in the HEALPix format (Górski et al., 1998).

We extrapolate the dust map to 53 GHz and 90 GHz with taking into account spatial variations of dust temperatures across the sky (Finkbeiner et al., 1999). We then cross-correlate the extrapolated maps with the DMR maps to confirm that the extrapolation is reasonable. We find that while the dust-correlated emission in the DMR 90 GHz map is consistent with the extrapolated dust emission, that in the DMR 53 GHz map is much larger than the extrapolated one. This is consistent with the anomalous microwave emission of Kogut et al. (1996a). To take the excess emission into account, we multiply our extrapolated 53 GHz maps by factors of 3.66, 2.59, and 2.45 for the 20° cut, the 25° cut, and the 30° cut, respectively. Note that we do not essentially need the correction for the excess emission, as it does not alter spatial distribution of the emission. Nevertheless, we do it for convenience of subsequent analyses.

We also extrapolate the synchrotron map to these two bands, assuming the spectrum of the source, $T(\nu) \propto \nu^{-2.9}$. We do not need the extrapolation of the synchrotron template map either, as the extrapolation does not alter spatial distribution of the emission in contrast to the dust template map in which the extrapolation does alter it. We find no significant correlation between the DMR maps and the extrapolated synchrotron maps at both 53 GHz and 90 GHz.

After coadding the extrapolated 53 and 90 GHz maps with the same weight as used for the DMR maps, we measure $B_{l_1 l_2 l_3}$ from the maps for the three different Galactic cuts, multiplying it by $G_{l_1} G_{l_2} G_{l_3}$ to take into account the DMR beam.

5.3.3 Constraints on non-linearity in inflation

We simultaneously fit the primary, dust, and synchrotron bispectra to the measured bispectrum on the DMR map. We use the least-squares method based on a χ^2 statistic defined by

$$\chi^2(f_j) \equiv \sum_{\alpha\alpha'} \left(I_\alpha^{\rm DMR} - \sum_j f_j I_\alpha^j \right) \left(C^{-1} \right)_{\alpha\alpha'} \left(I_{\alpha'}^{\rm DMR} - \sum_j f_j I_{\alpha'}^j \right). \tag{5.12}$$

I_α^j is a model bispectrum divided by $\left(\left\langle C_{l_1}^{\rm MC} \right\rangle \left\langle C_{l_2}^{\rm MC} \right\rangle \left\langle C_{l_3}^{\rm MC} \right\rangle \right)^{1/2}$, where j represents a certain component such as the primary, dust, and synchrotron. f_j is a fitting parameter for a component j, where $f_{\rm primary} \equiv f_{\rm NL}$ is the non-linear coupling parameter (Eq.(4.11)). $f_{\rm dust}$ and $f_{\rm sync}$ characterize amplitude of the foreground bispectra.

$C_{\alpha\alpha'}$ is the covariance matrix of the normalized bispectrum calculated from the Monte–Carlo simulations:

$$C_{\alpha\alpha'} \equiv \frac{1}{N-1} \sum_{i=1}^{N} \left(I_\alpha^{{\rm MC}(i)} - \left\langle I_\alpha^{\rm MC} \right\rangle \right) \left(I_{\alpha'}^{{\rm MC}(i)} - \left\langle I_{\alpha'}^{\rm MC} \right\rangle \right), \tag{5.13}$$

where $N = 50,000$ is the number of realizations. The bracket denotes an average over all realizations, $\left\langle I_\alpha^{\rm MC} \right\rangle \equiv N^{-1} \sum_i^N I_\alpha^{{\rm MC}(i)}$. Here, we have implicitly assumed the non-Gaussianity weak, so that we calculate the covariance matrix from Gaussian realizations.

As we have observed in the previous section, distribution of I_α is very much Gaussian; thus, $\chi^2(f_j)$ should obey the χ^2 distribution to good accuracy. Hence, minimizing $\chi^2(f_j)$ with respect to f_j gives the maximum-likelihood value of f_j as a solution to the normal equation:

$$f_j = \sum_i \left(F^{-1} \right)_{ji} \left[\sum_{\alpha\alpha'} I_\alpha^i \left(C^{-1} \right)_{\alpha\alpha'} I_{\alpha'}^{\rm DMR} \right], \tag{5.14}$$

where

$$F_{ij} \equiv \sum_{\alpha\alpha'} I_\alpha^i \left(C^{-1} \right)_{\alpha\alpha'} I_{\alpha'}^j. \tag{5.15}$$

We estimate statistical uncertainties of the parameters using the Monte–Carlo simulations; we obtain parameter realizations by substituting $I_\alpha^{\rm MC}$ for $I_\alpha^{\rm DMR}$ in equation (5.14).

Figure 5.5 plots the measured values of the non-linear coupling parameter, $f_{\rm NL}$, as well as the simulated realizations, for the three different Galactic cuts. The measured values are well within the cosmic variance: we place 68% confidence limits on $f_{\rm NL}$ as $|f_{\rm NL}| < 1.6 \times 10^3$, 1.7×10^3, and 2.0×10^3, for the 20°, 25°, and 30° cuts, respectively.

Figures 5.6 and 5.7 plot constraints on $f_{\rm dust}$ and $f_{\rm sync}$, respectively. There is no indication of either component contributing to the measured bispectrum significantly. The constraints are rapidly weakened as the Galactic cut is widened.

5.3.4 Null test of the normalized bispectrum

Using χ^2 defined by equation (5.12), we can test Gaussianity of the DMR map. While the minimization of $\chi^2(f_j)$ gives constraints on the parameters, a value of $\chi^2(f_j)$ tells us goodness-of-fit; $\chi^2(0)$ tests a hypothesis of the bispectrum being zero. When $\chi^2(0)$ is either significantly greater or smaller than those drawn from the simulations, we conclude that the DMR map is inconsistent with zero bispectrum.

$\chi^2(0)$ is similar to what several authors have used for quantifying statistical significance of non-Gaussianity in the DMR map (Ferreira et al., 1998; Magueijo, 2000; Sandvik and Magueijo, 2000). They use only diagonal terms of the covariance matrix; however, the matrix is diagonal only on the full sky. As lack of sky coverage correlates one mode to the others, we should include off-diagonal terms as well. We did so in equation (5.12).

Figure 5.8 compares $\chi^2_{\rm DMR}(0)$ with $\chi^2_{\rm MC}(0)$ for the different Galactic cuts. The measured values are $\chi^2_{\rm DMR}(0) = 475.6$, 464.8, and 460.2 for the corresponding cuts, respectively, while $\langle \chi^2_{\rm MC}(0) \rangle = 466$. We find the probability of $\chi^2_{\rm MC}(0)$ being larger than $\chi^2_{\rm DMR}(0)$ to be $P\left(\chi^2_{\rm MC} > \chi^2_{\rm DMR}\right) = 36.9\%$, 49.7%, and 54.2%, respectively.

We conclude that the DMR map is comfortably consistent with zero normalized bispectrum. We explain the claimed detection (Ferreira et al., 1998) by a statistical fluctuation without invoking the eclipse effect of Banday et al. (2000).

There is no evidence that the scatter of the normalized bispectrum is too small to be consistent with Gaussian, in contrast to the claim of Magueijo (2000) based on $\chi^2(0)$ derived from 8 modes. To clarify, our analysis does not reject the possibility that the CMB sky is non-Gaussian for only a small number of modes; however, in the absence of a theoretical motivation for limiting the analysis to a specific set of modes, we choose to treat all the bispectrum modes on an equal footing. Sandvik and Magueijo (2000) claim that the non-Gaussianity found by Magueijo (2000) does not spread to other modes. This is consistent with our result.

Incidentally, we plot in the figure 5.8 the χ^2 distribution for 466 degrees of freedom, χ^2_{466}, in filled circles; we find that the distribution of $\chi^2_{\rm MC}(0)$ is very similar to the χ^2_{466} distribution for a smaller cut as expected, while it becomes slightly broader for a larger cut for which the distribution of the normalized bispectrum at some modes deviates from Gaussian appreciably. Yet, we find that the $20° - 25°$ cuts reasonably retain the Gaussianity of the distribution of the normalized bispectrum.

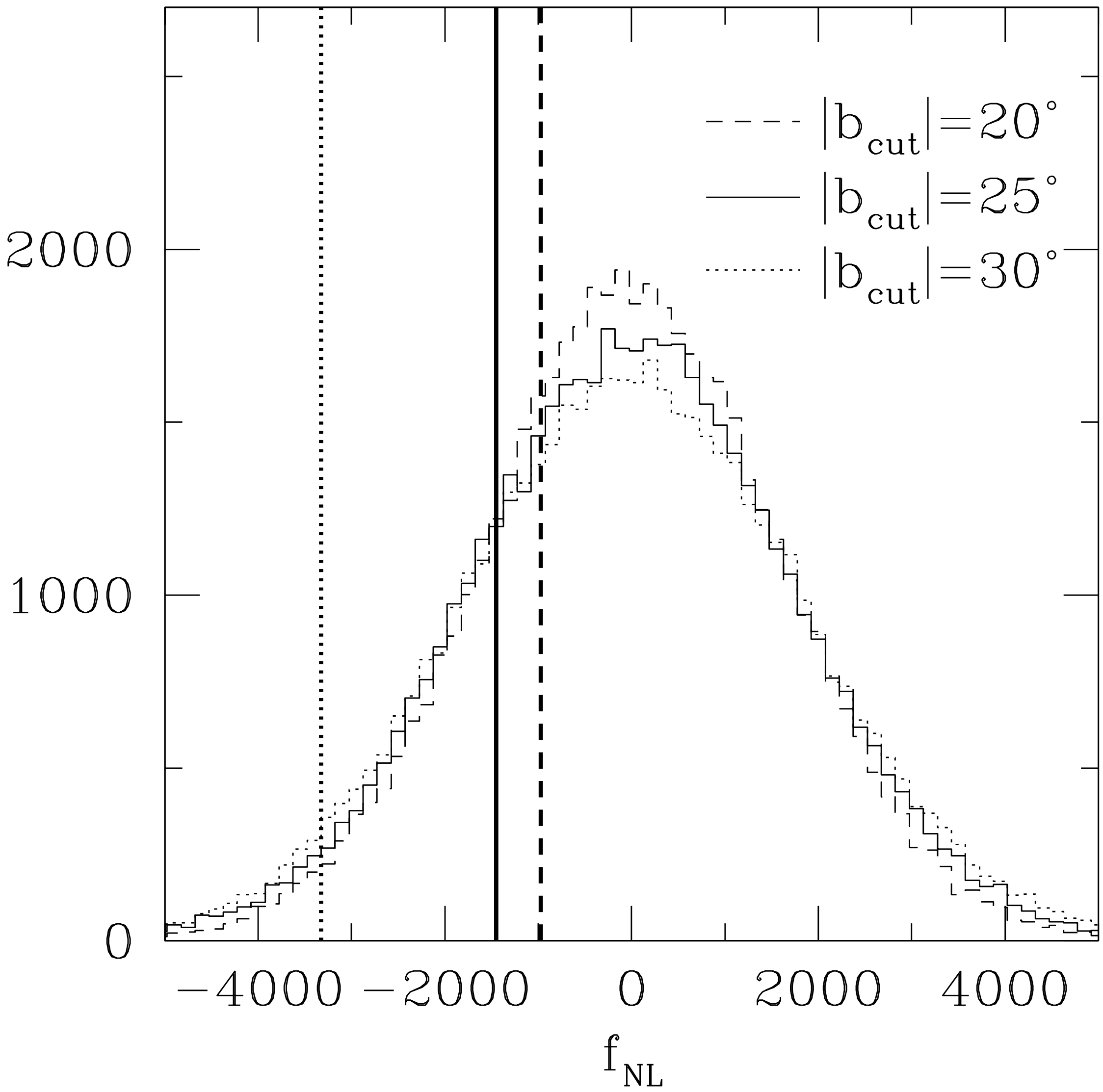

Figure 5.5: Constraint on Non-linearity in Inflation

DMR constraint on the non-linear coupling parameter, $f_{\rm NL}$, which characterizes non-linearity in inflation (Eq.(4.11)). The dashed, solid, and dotted lines represent the three different Galactic cuts as quoted in the figure. The thick vertical lines plot the measured values of $f_{\rm NL}$ from the *COBE* DMR maps, while the histograms plot those drawn from the Monte–Carlo simulations for each cut. 68% confidence limits on $f_{\rm NL}$ are $|f_{\rm NL}| < 1.6 \times 10^3$, 1.7×10^3, and 2.0×10^3 for the three Galactic cuts, respectively.

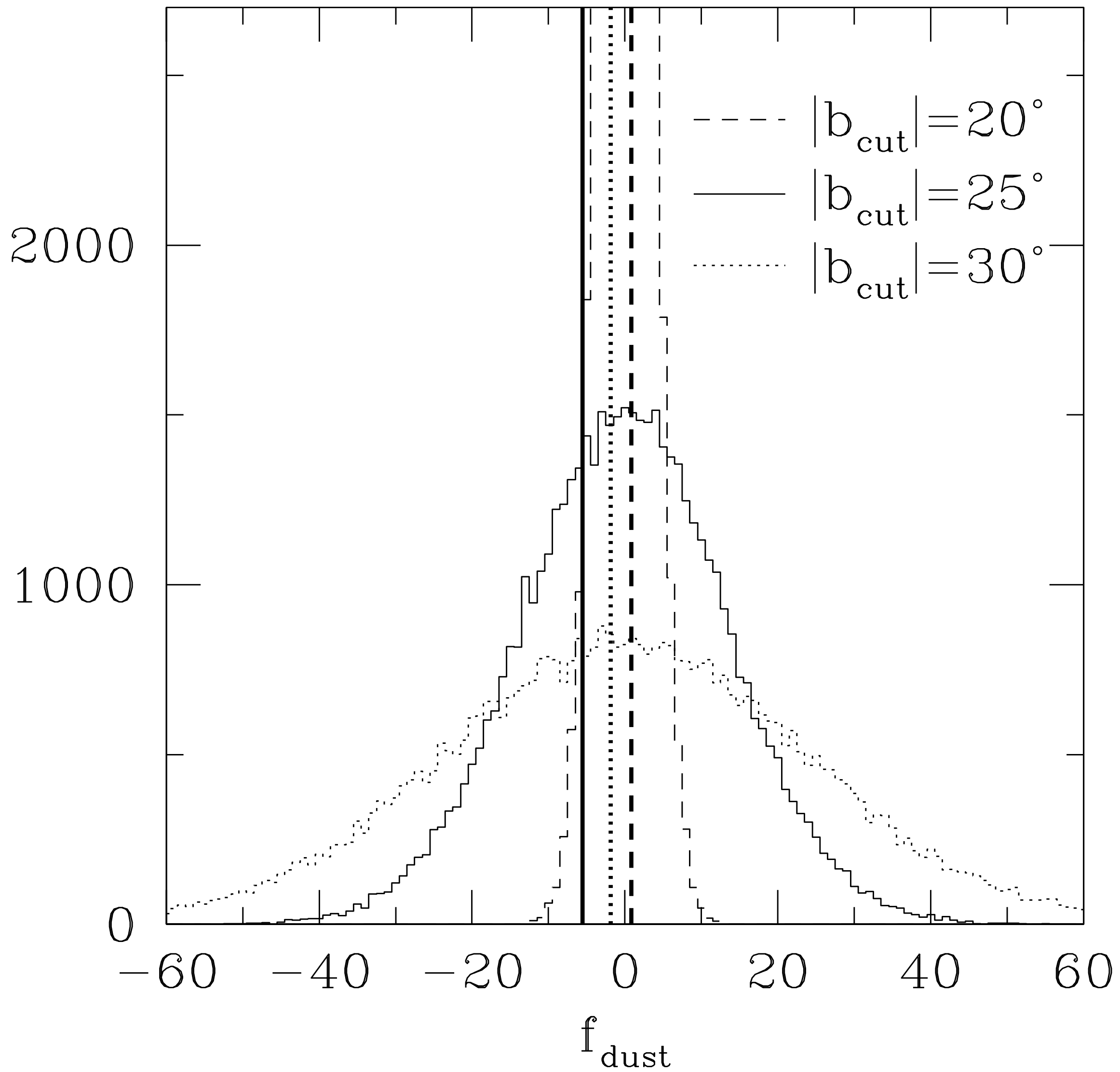

Figure 5.6: Constraint on Dust Bispectrum

DMR constraint on the amplitude of the interstellar dust bispectrum at high Galactic latitude, $f_{\rm dust}$. The meaning of the lines is the same as in figure 5.5.

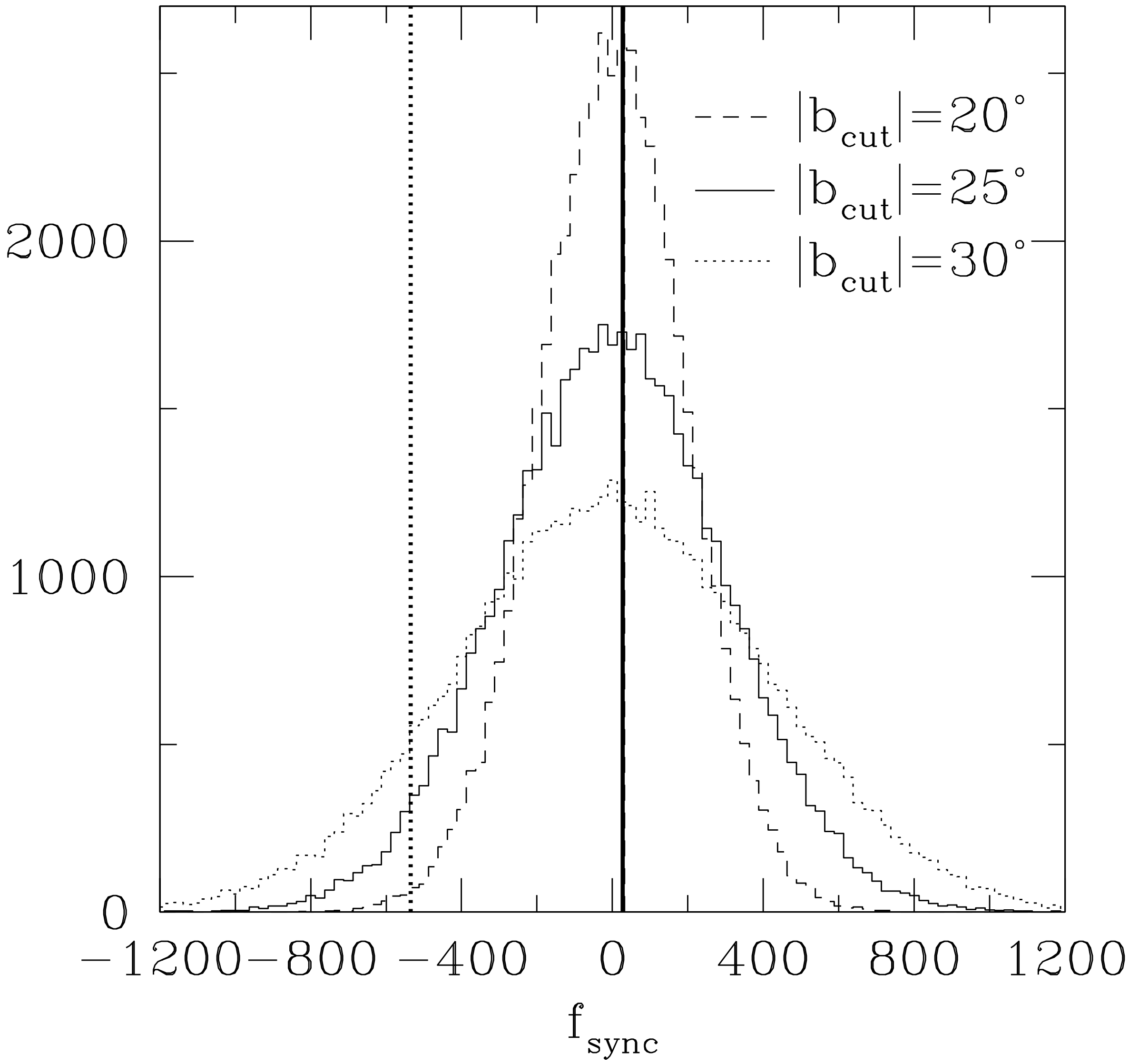

Figure 5.7: Constraint on Synchrotron Bispectrum

DMR constraint on the amplitude of the interstellar synchrotron bispectrum at high Galactic latitude, f_{sync}. The meaning of the lines is the same as in figure 5.5.

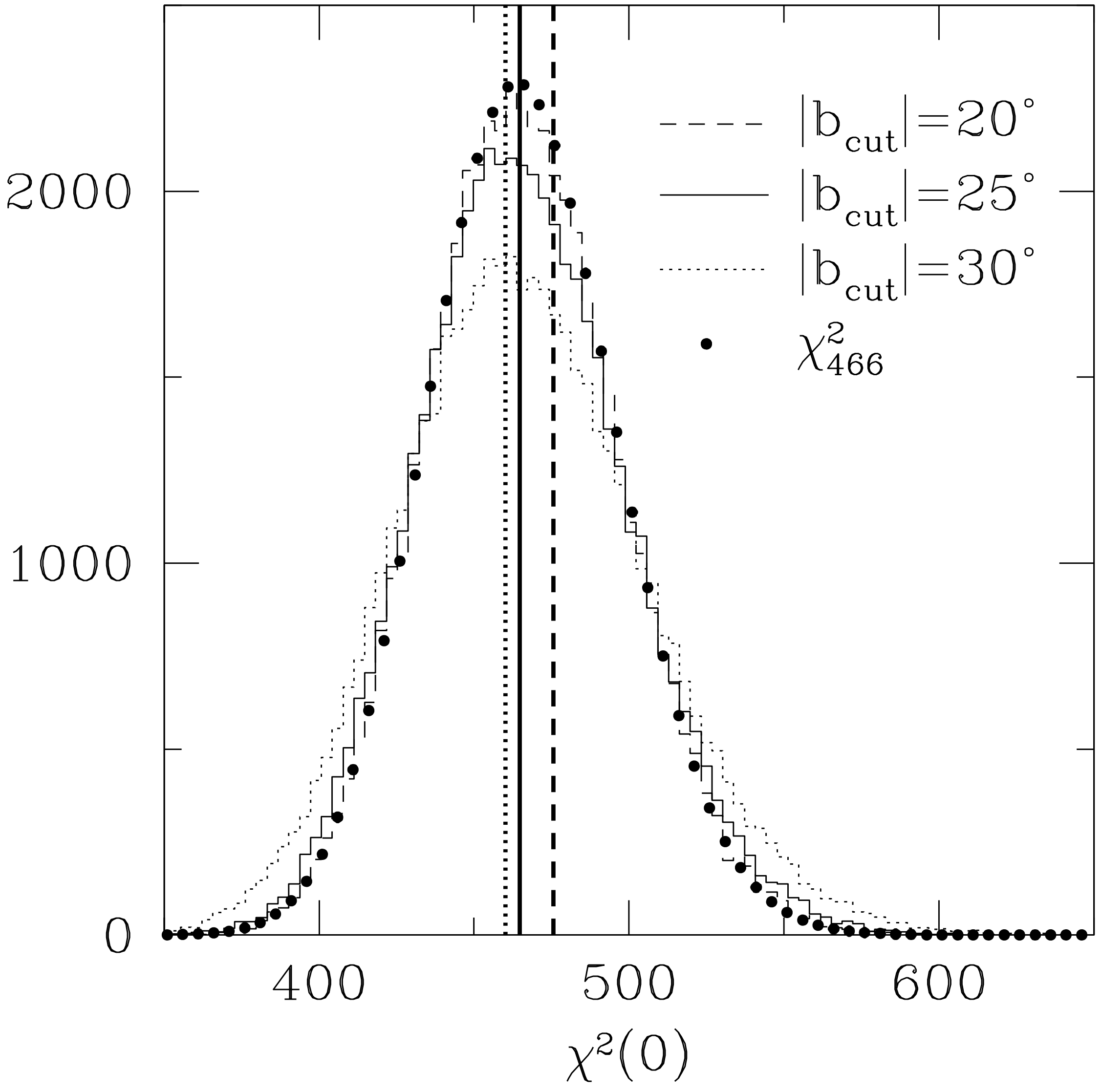

Figure 5.8: Null Test of Normalized Bispectrum

Testing hypothesis of the normalized bispectrum, $B_{l_1 l_2 l_3}/(C_{l_1} C_{l_2} C_{l_3})^{1/2}$, being zero in the *COBE* DMR four-year $53 + 90$ GHz sky map. The dashed, solid, and dotted lines represent the 20°, 25°, and 30° cuts, respectively. The thick vertical lines plot the measured $\chi^2(0)$, while the histograms plot those drawn from the Monte–Carlo simulations. The filled circles plot the χ^2 distribution for 466 degrees of freedom.

5.4 Discussion and Conclusions

In this chapter, we have measured all independent configurations of the angular bispectrum on the *COBE* DMR map, down to the DMR beam size. Using the most sensitive sky map to CMB, which combines the maps at 53 and 90 GHz, we test the Gaussianity of the DMR map.

We find that the normalized bispectrum, $B_{l_1 l_2 l_3} / \left(C_{l_1} C_{l_2} C_{l_3}\right)^{1/2}$, gives more robust test of Gaussianity than the bare bispectrum, $B_{l_1 l_2 l_3}$. We compare the measured data with the simulated realizations, finding the DMR map comfortably consistent with Gaussian. We explain the reported detection of the normalized bispectrum at $l_1 = l_2 = l_3 = 16$ (Ferreira et al., 1998) by a statistical fluctuation as an alternative to the "eclipse effect" proposition made in Banday et al. (2000).

We fit the predicted bispectra to the data, constraining the parameters in the predictions, which include the primary bispectrum from inflation and the foreground bispectra from interstellar dust and synchrotron emissions. We find that neither dust nor synchrotron emissions contribute to the bispectrum significantly.

We have obtained a weak constraint on the non-linear coupling parameter, $f_{\rm NL}$, that characterizes non-linearity in inflation. We interpret the constraint in terms of a single-field inflation as follows. According to the analysis of non-linear perturbations on super horizon scales (Salopek and Bond, 1990), we can explicitly calculate $f_{\rm NL}$ as

$$f_{\rm NL} = -\frac{5}{24\pi G}\left(\frac{\partial^2 \ln H}{\partial \phi^2}\right), \tag{5.16}$$

where H is the Hubble parameter during inflation. When applying the slow-roll conditions to an inflaton potential $V(\phi)$, we have $\partial \ln H/\partial\phi \approx (d\ln V/d\phi)/2$; thus, $f_{\rm NL}$ is on the order of curvature of a slow-roll potential, implying that $|f_{\rm NL}|$ should be smaller than 1 in slow-roll inflation. Therefore, the obtained constraint, $|f_{\rm NL}| < 1.6\times 10^3$, seems too weak to be interesting; however, any deviation from slow-roll could yield larger $|f_{\rm NL}|$, bigger non-Gaussianity.

The next generation satellite experiments, *MAP* and *Planck*, should be able to put more stringent constraints on $f_{\rm NL}$. In chapter 4, we have shown that *MAP* and *Planck* should be sensitive down to $|f_{\rm NL}| \sim 20$ and 5, respectively. We find that the actual constraint from *COBE* (figure 5.5) is much worse than the estimate. This is partly due to different cosmology used for the model, but mainly due to incomplete sky coverage; the statistical power of the bispectrum at low multipoles is significantly weakened by the Galactic cut. Since *MAP* and *Planck* probe much smaller angular scales, and their better angular resolution makes an extent of the Galactic cut smaller, the degradation of sensitivity should be minimal. Moreover, the improved frequency coverage of future experiments will aid in extracting more usable CMB pixels from the data. At this level of sensitivity, any deviation from slow-roll could give an interesting amount of the bispectrum, and *MAP* and *Planck* will put severe constraints on any substantial deviation from slow-roll.

While we have explored adiabatic generation of the bispectrum only, isocurvature perturbations from inflation also generate non-Gaussianity (Linde and Mukhanov, 1997; Peebles, 1997; Bucher and Zhu, 1997). They are in general more non-Gaussian than the adiabatic perturbations; it is worth constraining these models by the same strategy as we have done in this chapter.